EMT changes actin cortex rheology in a cell-cycle dependent manner

K. Hosseini,[1,2] A. Frenzel,[1,2] and E. Fischer-Friedrich[1,2,*]

[1] *Cluster of Excellence Physics of Life, Technische Universität Dresden, Dresden, Germany*
[2] *Biotechnology Center, Technische Universität Dresden, Dresden, Germany*

The actin cortex is a key structure for cellular mechanics and cellular migration. Accordingly, cancer cells were shown to change their mechanical properties based on different degrees of malignancy and metastatic potential. Epithelial-Mesenchymal transition (EMT) is a cellular transformation associated with cancer progression and malignancy. To date, a detailed study of the effects of EMT on the frequency-dependent viscoelastic mechanics of the actin cortex is still lacking. In this work, we have used an established AFM-based method of cell confinement to quantify the rheology of the actin cortex of human breast, lung and prostate epithelial cells before and after EMT in a frequency range of $0.02 - 2\,\mathrm{Hz}$. Interestingly, we find for all cell lines opposite EMT-induced changes in interphase and mitosis; while the actin cortex softens upon EMT in interphase, it stiffens in mitosis. Our rheological data can be accounted for by a rheological model with a characteristic time scale of slowest relaxation. In conclusion, our study discloses a consistent rheological trend induced by EMT in human cells of diverse tissue origin reflecting major structural changes of the actin cytoskeleton upon EMT.

Significance statement

The actin cortex is a key structure for cellular mechanics and cellular migration. Correspondingly, migratory cancer cells were shown to change their mechanical properties to a softer phenotype. EMT is a cellular transformation associated with cancer progression and malignancy. To date, a detailed study of the effects of EMT on the mechanics of the actin cortex is still lacking. In this work, we provide such a study for human breast, lung and prostate epithelial cells in dependence of the cell cycle stage. We observe a softening of the actin cortex in interphase but stiffening in mitosis upon EMT. In conclusion, our study discloses a consistent mechanical trend induced by EMT in human cells of diverse tissue origin.

Introduction

Many cells deform to function. Consequently, it is not surprising that cell mechanics is becoming more recognised to be a major factor in multiple diseases, such as cancer and cardiovascular, liver, and renal diseases [1, 2]. The actin cortex is a key contributor to passive material stiffness of cells, cellular ability to generate active forces and cell shape regulation [1, 3]. Hence, understanding actin cortex rheology is vital in understanding cell shape regulation. The actin cortex is a thin layer of a densely cross-linked actin polymer network beneath the plasma membrane of animal cells. It is a complex material with time-dependent viscoelastic mechanics [1, 3]. Further, it is subject to an intrinsically generated active contractile tension; this tension stems from the action of molecular motor proteins (myosins), which act as active force dipoles in the actin polymer meshwork [3]. Molecular constituents of the actin cortex are subject to dynamic turnover (e.g. polymerisation and depolymerisation) - a feature that inevitably contributes to elastic relaxation processes in the material as well as to a time-limited shape memory [3].

Epithelial cells line the surface of organs and internal cavities in animals [4]. If epithelial cells have undergone carcinogenic transformations, they constitute a type of cancer called carcinoma. Carcinoma make up the majority ($\sim 85\%$) of malignant tumors in humans [5]. The Epithelial-Mesenchymal transition (EMT) is a cellular transition that converts polarised stationary epithelial cells into migratory mesenchymal cells. It is known to be a hallmark of cancer progression and malignancy in carcinoma [6–8]. EMT is commonly linked to early steps in metastasis promoting cell migration and cancer cell invasiveness [6–9]. Furthermore, EMT was shown to give rise to major changes in the molecular regulation of the actin cortex; the cytoskeletal regulator proteins RhoA and Rac1 undergo characteristic activity changes upon EMT indicating EMT-induced changes in the polymerisation process and the structure of the actin cytoskeleton [10–13].

While mechanical changes of cancer cells have been documented in many studies [10, 14–20], a detailed study of EMT-induced rheological changes of the actin cortex is still lacking. Here, we present such a rheological characterisation in dependence of malignant potential, EMT and cell-cycle stage. We utilise an established cell mechanical assay based on cell confinement with a wedged cantilever of an atomic force microscope (AFM) [10, 21, 22]. In this measurement setup, initially round mitotic or suspended interphase cells are uniaxially compressed between two parallel surfaces and exposed to time-periodic cell height oscillations [10, 22] (Fig. 1a,b). As was shown before, the resulting mechanical response of the cell in this setup is dominated by the actin cortex, see Fig. 4 in [22] and Fig. S7 in [10]. Correspondingly, we use the measured AFM force readout to estimate active cortical tension and the complex elastic modulus of the actin cortex in dependence of frequency in interphase and mitosis [10, 21, 22].

Results

In the first set of experiments, we investigated three breast epithelial cell lines with increasing degree of malignant potential. The first cell line, MCF-10A, represents healthy breast epithelial cells. The second cell line, MCF-7, are breast carcinoma cells with epithelial phenotype. The third cell line, MDA-MB231, are also breast carcinoma cells with mesenchymal-like phenotype [14, 23–25]. These three cell lines exhibit a graded increase of migration ability and invasiveness, with MCF-10A showing the smallest, MCF-7 an intermediate and MDA-MB231 the largest migration ability [26–28]. Correspondingly, a graded increase of malignant potential is associated to these cell lines [14, 15, 23]. The actin cortex plays a major role in enabling cell migration [3, 29]. Therefore, we performed a frequency-dependent analysis of the rheology of the actin cortex of all three cell lines, to see whether altered migratory potential is reflected in changes of cellular mechanics.

Results of our rheological analysis of the three cell lines are presented in Fig. 1. We find that rheological trends are qualitatively similar to cortical rheology observed for the actin cortex of HeLa cells [22]; at high frequencies, the storage modulus G' clearly dominates (Fig. 1c,e). However, in the low frequency regime, storage and loss modulus are of similar magnitude, indicating a higher fluid-like component. Frequency-dependence of storage and loss moduli are well described by a rheological model that anticipates a constant relaxation spectrum up to a slowest cut-off relaxation time scale (see Eqn. (2) and (3) in Materials and Methods). Corresponding model fits to measured storage and loss moduli are depicted as solid lines in (Fig. 1c,e). Fitting parameters τ_{max}, K_h and η are shown in the caption of Fig. 1, where τ_{max} quantifies the slowest relaxation time scale, K_h rates the mechanical strength of relaxation modes and η captures an additional purely viscous, linear contribution to the loss modulus at high frequencies.

For interphase cells, we see a clear trend of decreasing storage and loss moduli in dependence of increasing malignant potential (Fig. 1, from left to right in panel c). By contrast, for mitotic cells, we find the opposite trend of increasing storage and loss modulus in dependence of increasing malignant potential (Fig. 1, from left to right in panel e). Corresponding loss tangents G''/G' for the cortex of interphase and mitotic cells are presented in panels Fig. 1d,f.

Solid lines describe model loss tangents as inferred by Eqn. (2) and (3) using parameters from fits to measured storage and loss moduli as shown in Fig. 1c,e. Unlike previously reported [23], we do not see a particular trend of the loss tangent of cells in dependence of malignant potential, see Fig. 1d,f. Boxplots of cortical stiffness quantified by $|G^*|$ and phase shift $\tan^{-1}(G''/G')$ measured at a frequency of 1 Hz as well as active cortical tension are presented in Fig. S1a-c. In conclusion, we observe here a trend of decreasing interphase cortical moduli and increasing mitotic cortical moduli in conjunction with increasing malignant potential. Similar trends for interphase cell mechanics in dependence of malignancy were reported previously [10, 14–20]. Furthermore, stiffening of mitotic cells upon cancerous transformation and EMT has been shown in [10, 30].

EMT is known to be a hallmark of cancer progression and malignancy [6, 31]. Therefore, we wanted to test to which extent actin cortex rheology is influenced by EMT-associated cortex remodelling. Our previous study reported EMT-induced cell-cycle dependent changes of cortical mechanics in breast epithelial cells sampled at a frequency of

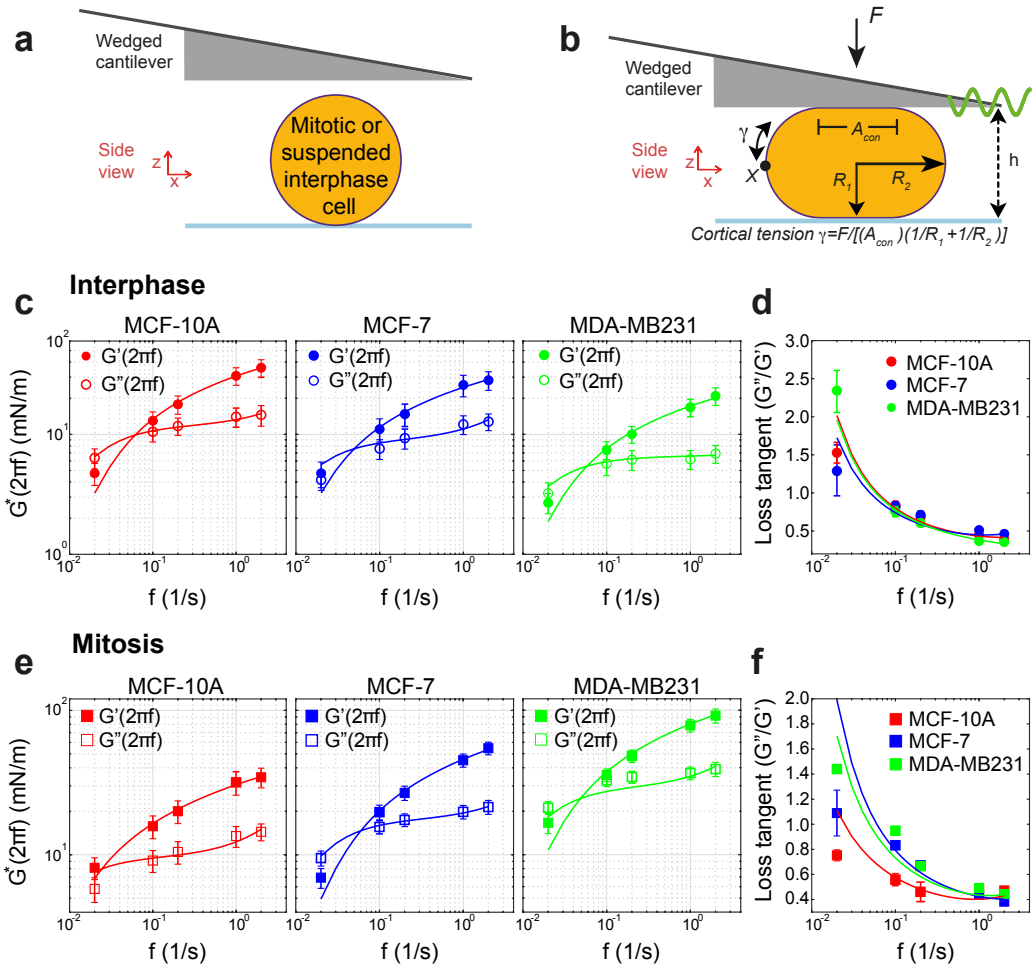

Figure 1. Mechanical phenotyping of the actin cortex for suspended interphase and STC-arrested mitotic MCF-10A, MCF-7 and MDA-MB231 cells. a-b) Schematic of experimental setup. Non-adherent interphase or mitotic cells (yellow sphere) are confined by a wedged AFM cantilever. Dynamic cantilever height changes deform the cell around a mean confined reference shape while recording cellular force response through AFM-detected cantilever deflection. c) Averaged two-dimensional complex elastic moduli of suspended interphase MCF-10A, MCF-7 and MDA-MB231 cells. d) Loss tangents corresponding to data in panel c. e) Averaged two-dimensional complex elastic moduli of MCF-10A, MCF-7 and MDA-MB231 cells in mitotic arrest. (Storage modulus: filled-circles, loss modulus: open circles) f) Loss tangents corresponding to data in panel e. Obtained fit parameters for data in panels c and e were: MCF-10A interphase: $K_h = 7.525$ mN/m, $\tau_{max} = 49.284$ s and $\eta = 0.252$ Pa s, MCF-7 interphase: $K_h = 5.76$ mN/m, $\tau_{max} = 11.51$ s and $\eta = 0.338$ Pa s, MDA-MB231 interphase: $K_h = 4.2$ mN/m, $\tau_{max} = 9.59$ s and $\eta = 0.011$ Pa s, MCF-10A mitosis: $K_h = 6.129$ mN/m, $\tau_{max} = 23.242$ s and $\eta = 0.431$ Pa s, MCF-7 mitosis: $K_h = 11.225$ mN/m, $\tau_{max} = 9.445$ s and $\eta = 0.0.3232$ Pa s and MDA-MB231 mitosis: $K_h = 18.6543$ mN/m, $\tau_{max} = 11.6887$ s and $\eta = 0.9314$ Pa s. Number of cells analysed: interphase: MCF-10A n=16, MCF-7 n=19, MDA-MB231 n=12, mitosis: MCF-10A n=32, MCF-7 n=38 and MDA-MB231 n=41. Error bars indicate the standard error of the mean.

1 Hz. However, a complete characterisation of cortical rheological changes upon EMT is lacking. To this end, we mechanically sampled the actin cortex of MCF-7 and MCF-10A cells before and after pharmacologically induced EMT (Fig. 2). EMT was induced by TPA- or TGF-β1-treatment as described before, see [10] and Materials and Methods. Measurements were performed on non-adherent interphase cells and cells in mitotic arrest for frequencies between 0.02 - 2 Hz. Obtained estimates of cortical complex elastic moduli in dependence of frequency are shown in Fig. 2. We find that moduli of non-adherent interphase MCF-7 and MCF-10A cells are lowered upon EMT at all frequencies measured. Vice versa, complex elastic moduli increased at all frequencies in mitotic cells of both cell lines. Data points were fitted with our rheological model as given by Eqn. (2) and (3) (solid lines in all panels of Fig. 2). Overall, we find good agreement with our measurements. Corresponding fitting parameters τ_{max}, K_h and η are shown in the caption of Fig. 2. The loss tangents showed no EMT-related trend in mitotic and interphase MCF-10A and MCF-7 cells (Fig. S2a-b).

So far, we only tested the influence of EMT on cortical mechanics in breast epithelial cells. To investigate if EMT-associated rheological changes are conserved in cells of other tissue origin, we applied our assay to the cell lines DU-145 and A-549 originating from explanted prostate carcinoma [32] and lung tumor tissue [33], respectively. Both cell lines show an epithelial phenotype in standard media. Using an established protocol, we induced EMT pharmacologically through TGF-β1 treatment [34, 35], see Materials and Methods. In order to verify EMT in our treated cells, we performed immunoblotting and observed the characteristic decrease in E-cadherin and a corresponding increase in N-cadherin and Vimentin (Fig. S3a-b). As before, we measured actin cortex rheology before and after EMT in non-adherent interphase and mitotic cells obtaining complex elastic moduli as depicted in Fig. 3a-d. Analogous to breast epithelial cell lines, we find that complex elastic moduli of non-adherent interphase cells are lowered upon EMT (Fig. 3a-b) while moduli of mitotic cortices increased at all frequencies (Fig. 3c-d). Data points were fitted with our rheological model as given by Eqn. (2) and (3) (solid lines in all panels of Fig. 3). Again, we find on average good agreement with our measurements. Fitting parameters τ_{max}, K_h and η of averaged rheological data are shown in the

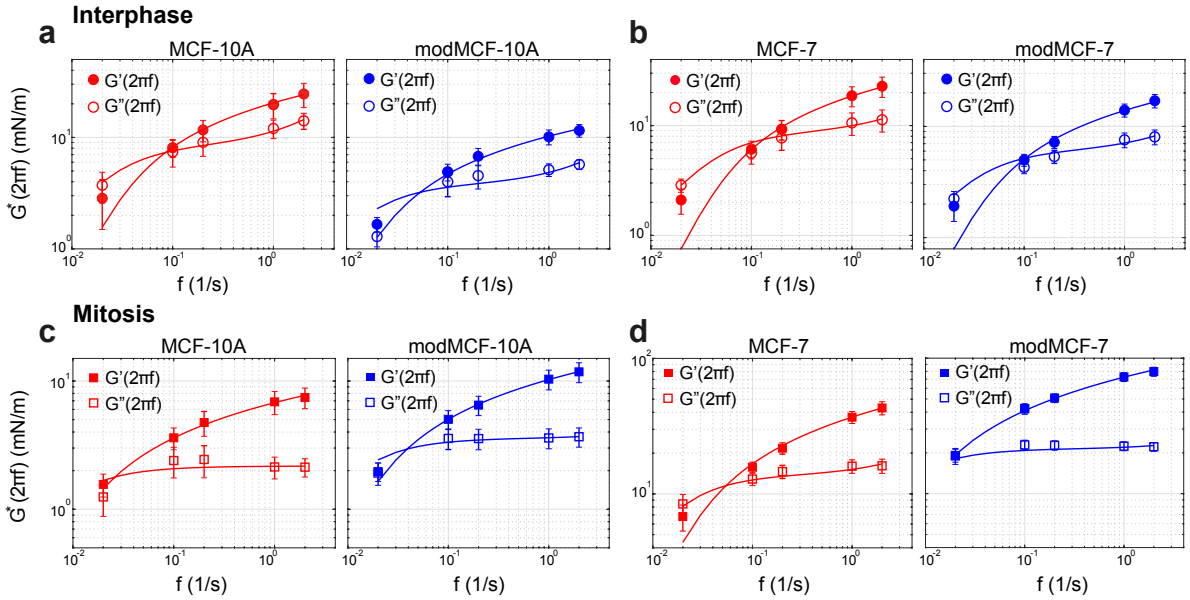

Figure 2. EMT-induced actin cortex mechanical changes of MCF-10A and MCF-7 cells. a-b) Averaged two-dimensional complex elastic moduli of suspended interphase MCF-10A and MCF-7 cells upon EMT. c-d) Averaged two-dimensional complex elastic moduli of MCF-10A and MCF-7 cells in mitotic arrest before and after EMT. (Storage modulus: filled-circles, loss modulus: open circles) (Post-EMT cells are referred to as modMCF-10A and modMCF-7, respectively.) Obtained fit parameters for data in panels a-c were: MCF-10A interphase: $K_h = 5.38$ mN/m, $\tau_{max} = 7.067$ s and $\eta = 0.484$ Pa s, modMCF-10A interphase: $K_h = 2.4318$ mN/m, $\tau_{max} = 10.775$ s and $\eta = 0.17$ Pa s, MCF-7 interphase: $K_h = 5.85$ mN/m, $\tau_{max} = 4.431$ s and $\eta = 0.226$ Pa s, modMCF-7 interphase: $K_h = 3.9$ mN/m, $\tau_{max} = 5.63$ s and $\eta = 0.171$ Pa s, MCF-10A mitosis: $K_h = 13.824$ mN/m, $\tau_{max} = 21.39$ s and $\eta = 1.41$ Pa s, modMCF-10A mitosis: $K_h = 22.77$ mN/m, $\tau_{max} = 14.36$ s and $\eta = 0.1$ Pa s, MCF-7 mitosis: $K_h = 8.827$ mN/m, $\tau_{max} = 10.39$ s and $\eta = 0.23$ Pa s and modMCF-7 mitosis: $K_h = 13.66$ mN/m, $\tau_{max} = 31.9$ s and $\eta = 0.1$ Pa s. Number of cells analysed: interphase: MCF-10A n=16, modMCF-10A n=18, MCF-7 n=20, modMCF-7 n=18, mitosis: MCF-10A n=21, modMCF-10A n=23, MCF-7 n=23 and modMCF-7 n=22. Error bars indicate standard error of the mean.

caption of Fig. 3. Corresponding loss tangents showed no clear EMT-induced trend in interphase and mitotic DU-145 and A-549 cells (Fig. S3c-d). Furthermore, we present boxplots of cortical stiffness quantified by $|G^*|$ and phase shift $\tan^{-1}(G''/G')$ measured at frequency of 1 Hz as well as active cortical tension are presented in Fig. 3e-g. Similar to breast epithelial cell lines, we find a significant EMT-induced cell mechanical trend of decreased cortical stiffness and active cortical tension in interphase DU-145 and A-549 cells and the opposite trend in mitosis (Fig. 3e-g, lower panels).

For EMT-related rheological measurements on MCF-10A, MCF-7, DU-145 and A-549 (see Fig. 2, 3), rheological fitting

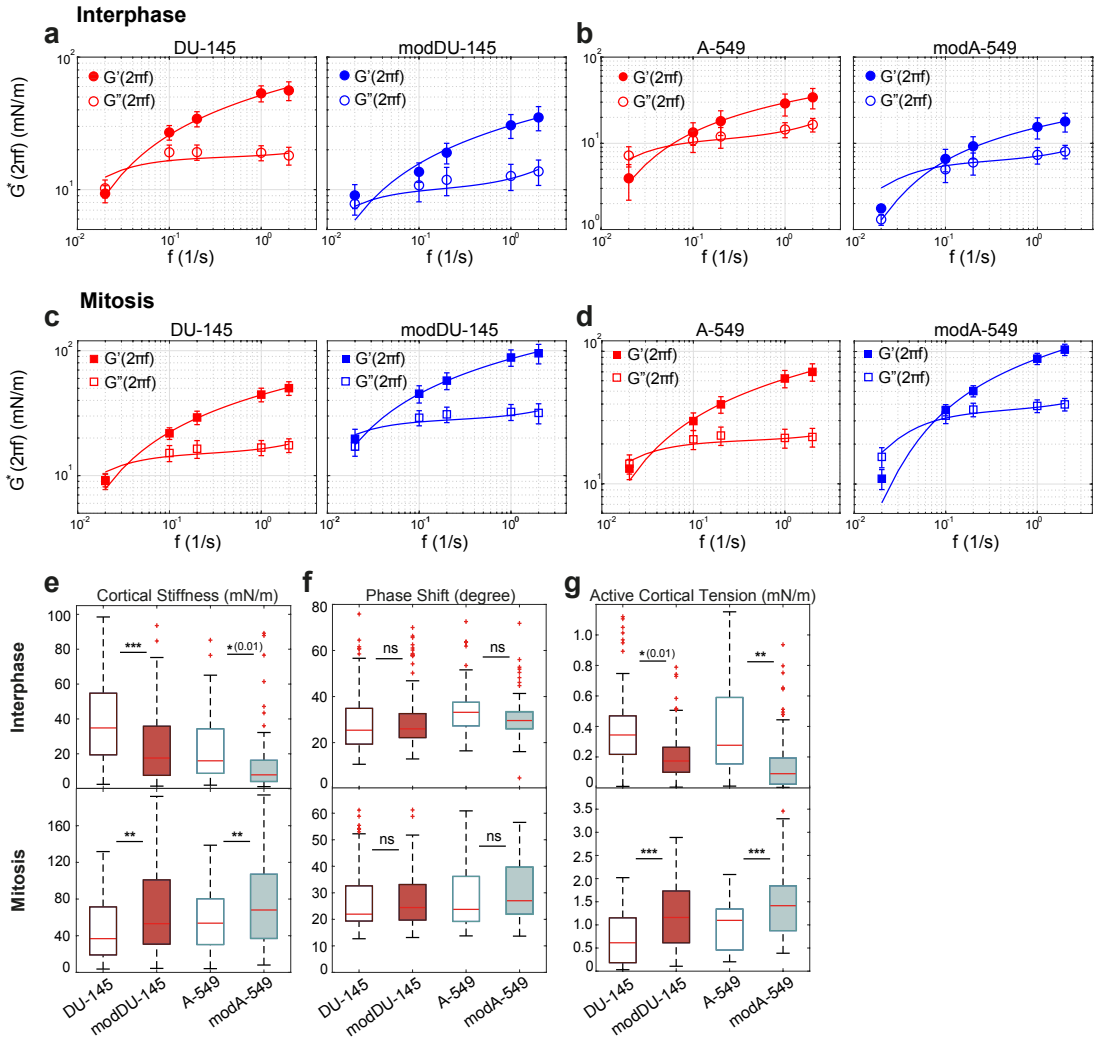

Figure 3. EMT-induced actin cortex mechanical changes of DU-145 and A549 cells. a-b) Averaged two-dimensional complex elastic moduli of suspended interphase DU145 and A-549 cells upon EMT. c-d) Averaged two-dimensional complex elastic moduli of DU145 and A-549 cells in mitotic arrest before and after EMT. (Storage modulus: filled-circles, loss modulus: open circles) e-g) Boxplots of cortical stiffness $|G^*|$ (e), phase shift (f) and active cortical tension (g) measured for suspended interphase cells (top row) and cells in mitotic arrest (bottom row) before and after EMT at 1 Hz frequency. (Post-EMT cells are referred to as modDU-145 and mod-A-549, respectively. Obtained fit parameters in panels a-d were: DU145 interphase: $K_h = 11.2$ mN/m, $\tau_{max} = 15.91$ s and $\eta = 0.102$ Pa s, modDU145 interphase: $K_h = 6.43$ mN/m, $\tau_{max} = 18.18$ s and $\eta = 0.331$ Pa s, A-549 interphase: $K_h = 7.05$ mN/m, $\tau_{max} = 10.44$ s and $\eta = 0.467$ Pa s, modA-549 interphase: $K_h = 3.95$ mN/m, $\tau_{max} = 7.61$ s and $\eta = 0.156$ Pa s, DU145 mitosis: $K_h = 9.6$ mN/m, $\tau_{max} = 16.11$ s and $\eta = 0.227$ Pa s, modDU145 mitosis: $K_h = 17.85$ mN/m, $\tau_{max} = 19.85$ s and $\eta = 0.409$ Pa s, A-549 mitosis: $K_h = 13.51$ mN/m, $\tau_{max} = 15.47$ s and $\eta = 0.147$ Pa s and modA-549 mitosis: $K_h = 22.96$ mN/m, $\tau_{max} = 7.44$ s and $\eta = 0.383$ Pa s. Number of cells analysed (a-d): interphase: DU145 n=24, modDU145 n=22, A-549 n=22, modA-549 n=24, mitosis: DU145 n=18, modDU145 n=17, A-549 n=24 and modA-549 n=24, (e-g): interphase: DU145 n=36, modDU145 n=36, A-549 n=35, modA-549 n=39, mitosis: DU145 n=34, modDU145 n=34, A-549 n=34 and modA-549 n=29. Error bars indicate standard error of the mean. n.s.: $p > 0.05, * : p < 0.05, ** : p < 0.01, *** : p < 0.001$).

parameters as well as active cortical tension γ_{act} obtained for individual cells are summarised in Table I. Furthermore, Fig. 4 shows corresponding boxplots of obtained parameter distributions. In interphase, for all cell lines considered, the modulus K_h and active cortical tension decreases upon pharmacological EMT induction (Fig. 4a,d, top). By contrast, for all cell lines, K_h and active cortical tension γ_{act} increase upon EMT in mitosis (Fig. 4a,d, bottom). The characteristic time scale τ_{max} shows no consistent EMT-related trend (Fig. 4b); τ_{max} does not change significantly in interphase cells for all cell lines and in mitotic MCF-10A and DU-145 cells. In mitotic MCF-7 cells, τ_{max} increases upon EMT indicating an EMT-triggered solidification in mitosis. Vice versa, in mitotic A-549 cells, τ_{max} decreases upon EMT indicating an EMT-triggered fluidization in mitosis. Interestingly, we find that EMT-induced changes of τ_{max} tend to be opposite in interphase and mitosis. However, the direction and magnitude of the change varies between cell lines. Also the viscous contribution η shows no consistent trend upon EMT (Fig. 4c); In MCF-10A and A-549 interphase cells, this viscosity decreases on average (Fig. 4c, top). In addition, we see an increase of η in mitotic A-549 cells. These findings might point to a change of cytoplasmic viscosity upon EMT through bulk cytoskeleton softening in interphase and stiffening in mitosis in respective cell lines.

Discussion

In this study, we investigated the influence of EMT on frequency-dependent actin cortex rheology of human cells in interphase and mitosis. To this end, we utilised an established AFM-based cell-confinement assay which was previously shown to provide a characterisation of the complex elastic modulus and the active tension of the actin cortex [10, 21, 22, 36]. The presence of active stresses in a material can confound the values of the elastic modulus

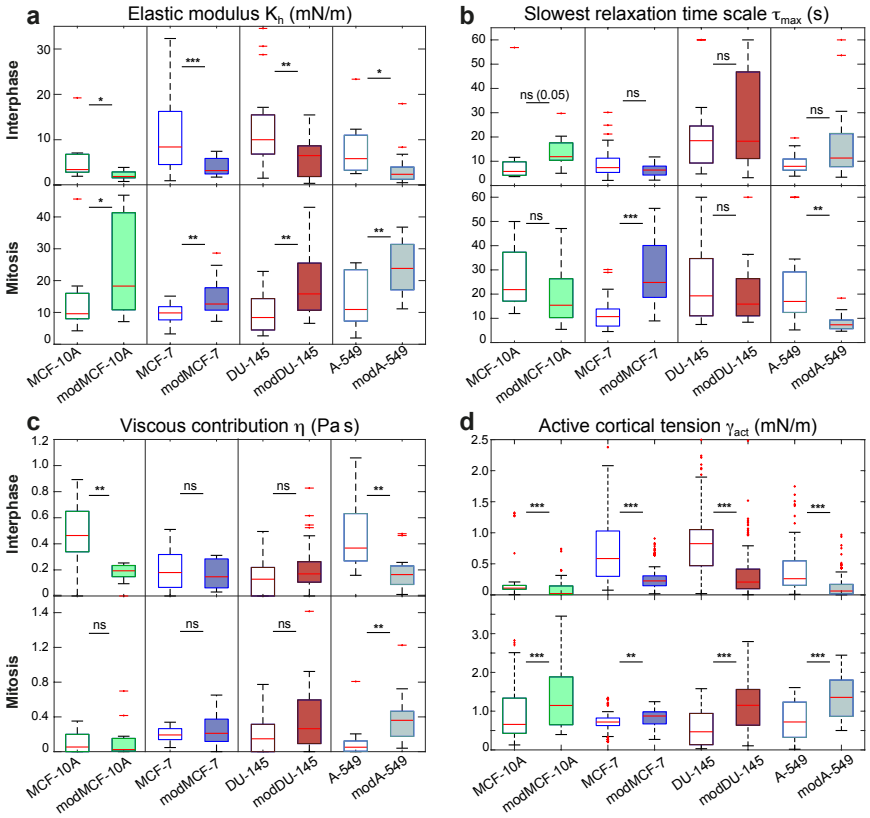

Figure 4. a-d) Boxplots indicating the distribution of fitting parameters (a) K_h, (b) τ_{max} and (c) η as well as (d) active cortical tension γ_{act} for measured MCF-10A, MCF-7,DU-145, A-549 interphase and mitotic cells before and after EMT. (Post-EMT cells are referred to as modMCF-10A, modMCF-7, modDU-145 and mod-A-549, respectively. Number of cells analysed (a-d): interphase: MCF-10A n=16, modMCF-10A n=18, MCF-7 n=20, modMCF-7 n=18, DU-145 n=24, modDU-145 n=22, A-549 n=22, modA-549 n=24, mitosis: MCF-10A n=21, modMCF-10A n=23, MCF-7 n=23, modMCF-7 n=22, DU-145 n=18, modDU-145 n=17, A-549 n=24 and modA-549 n=24. n.s.: $p > 0.05, * : p < 0.05, ** : p < 0.01, *** : p < 0.001$.)

obtained from mechanical measurements [37–39]. Our assay avoids this effect by separating active and passive cortical stresses in the data analysis, thus, reporting active cortical tension and cortical viscoelastic moduli as independent parameters [22]. We find that all our rheological measurements of the actin cortex are well captured by a simple rheological model that anticipates a constant spectrum of relaxation time scales in the material up to a slowest relaxation time scale τ_{max}, see solid lines in Fig. 1, 2 and 3. This model is consistent with the idea that the turnover of different actin cross-linkers contributes multiple cortical relaxation time scales [40, 41]. Naturally, cortical relaxation times scales must be bounded by the time scale of turnover of polymerised actin in the cortex. In fact, our estimated range for the largest relaxation time scale $\tau_{max} \approx 5$-$25\,\mathrm{s}$ agrees reasonably well with actin turnover time scales predicted by photobleaching experiments at the cortex [3, 10, 42].

Inducing EMT in epithelial cell lines derived from breast, lung and prostate tissue, we observed a general trend of a reduction of actin cortex elastic moduli in interphase cells and a decrease of active cortical tension. By contrast, we found that moduli of the actin cortex of mitotic cells are generally higher than those of interphase cells with a distinct increase upon EMT. Furthermore, mitotic cells develop a higher active cortical tension upon EMT, see Fig. 2 and 3. By comparison, we find that an increase in malignant potential in breast epithelial cells gives the same trend as EMT induction (reduction in interphase, increase in mitosis), see Fig. 1 and S1.

Previously, many cell-mechanical studies have reported interphase cell softening in correlation with an increase in malignancy potential [10, 14–20, 30]. Furthermore, in mitotic cells, it was shown that Ras-activation enhances mitotic stiffness as measured by AFM indentation [30]. As EMT is a hallmark of cancer progression and malignancy, our findings are consistent with these earlier studies. Other studies have monitored cellular stiffness changes upon EMT. Osborne *et al.* observed cell-softening upon EMT in isolated adherent murine breast epithelial cells using adherent magnetic beads deflected by a magnetic tweezer [43]. Interestingly, Schneider *et al.* reported effective cell-stiffening upon EMT in adherent sheets of murine breast epithelial cells using AFM indentation at the apical cell apex [44]. Here, the authors attribute their findings to an increased actin cytoskeletal contribution in cellular force response after EMT rather than to stiffening of the actin cytoskeleton itself. A corresponding reorganisation and redistribution of actin cytoskeleton upon EMT was shown by Haynes *et al.* [45]. Our previous study on breast epithelial cells also showed a softening of interphase and a stiffening of mitotic cells' cortices upon EMT measured at a single frequency of $1\,\mathrm{Hz}$.

The cytoskeletal regulator proteins Rac1 and RhoA have been shown to undergo major activity changes upon EMT [10–13]. In particular, activity changes of Rac1 might account for the cell-cycle dependent mechanical changes of the actin cortex by an as yet unknown downstream mechanism [10].

In summary, we showed in this study that measured actin cortex mechanics is captured by a universal rheological model described by a constant relaxation spectrum of time scales up to a slowest relaxation time scale τ_{max} which we determined to be in the range of $5 - 25\,\mathrm{s}$. Our data suggest that this rheological model is conserved for cells from different tissue origin and throughout the cell-cycle. The cancer-related cellular transformation EMT leads to a roughly universal downscaling of viscoelastic moduli of the cortex in interphase and an opposite upscaling of moduli in mitosis. Concomitantly, active cortical tensions decrease in interphase and increase in mitosis upon EMT. We conclude that these EMT-induced rheological changes likely reflect major changes in the organisation and structure of the actin cytoskeleton upon EMT. These changes may also be at the heart of EMT-induced altered biological function such as cellular migration and mitotic rounding.

Cell type	K_h (mN/m)	p-value	τ_{max} (s)	p-value	η (Pa s)	p-value	γ_{act} (mN/m)	p-value	n(#)
MCF-10A interphase	3.42	1	5.81	1	0.46	1	0.11	1	16
modMCF-10A interphase	1.89	0.0101	11.89	0.0350	0.19	0.0030	0.023	0.0005	18
MCF-10A mitosis	9.59	1	21.85	1	0.053	1	0.66	1	21
modMCF-10A mitosis	18.28	0.0355	15.40	0.0649	0.024	0.8937	1.15	0.0009	23
MCF-7 interphase	8.40	1	7.38	1	0.180	1	0.58	1	20
modMCF-7 interphase	3.20	0.0168	6.38	0.3908	0.15	0.5965	0.22	0.0015	18
MCF-7 mitosis	9.85	1	10.71	1	0.19	1	0.72	1	23
modMCF-7 mitosis	12.64	0.0077	24.81	0.00004	0.21	0.4731	0.87	0.0096	22
DU-145 interphase	10.00	1	18.48	1	0.13	1	0.82	1	24
modDU145 interphase	6.50	0.0038	18.26	0.6580	0.17	0.1146	0.21	0.0002	22
DU-145 mitosis	8.40	1	19.28	1	0.15	1	0.47	1	18
modDU145 mitosis	15.82	0.0048	15.87	0.9080	0.26	0.1331	1.15	0.0013	17
A-549 interphase	5.83	1	7.91	1	0.37	1	0.26	1	22
modA-549 interphase	2.38	0.0126	11.32	0.1441	0.16	0.0009	0.062	0.0004	24
A-549 mitosis	10.92	1	19.97	1	0.05	1	0.72	1	24
modA-549 mitosis	23.83	0.0063	7.33	0.0022	0.36	0.0012	1.36	0.0006	24

Table I. Rheological parameters of different EMT-induced cell lines in suspended interphase and mitosis. The values represent median values of elastic modulus K_h, slowest relaxation time τ_{max}, viscous contribution η and active cortical tension γ_{act} along with the number of cells analysed corresponding to measurements in Fig. 4a-c.

Materials and Methods

Cell culture.
The cultured cells were maintained as follows: MCF-7, DU-145 and A-549 cells were grown in RPMI-1640 medium (PN:2187-034, life technologies) supplemented with 10% (v/v) fetal bovine serum, 100 μg/mL penicillin, 100 μg/ml streptomycin (all Invitrogen) at 37°C with 5% CO_2. MCF-10A cells were cultured in DMEM/F12 medium (PN:11330-032, Invitrogen) supplemented with 5% (v/v) horse serum (PN:16050-122, Invitrogen), 100 μg/mL penicillin, 100 μg/mL streptomycin (all Invitrogen), 20 mg/mL epidermal growth factor (PN:AF-100-15, Peprotech), 0.5 mg/mL hydrocortisone (PN:H-0888, Sigma), 100 ng/mL cholera toxin (PN:C-8052, Sigma), 10 μg/mL insulin (PN:I-1882, Sigma) at 37°C with 5% CO_2. In MCF-7 cells, EMT was induced by incubating cells in medium supplemented with 100 nM 12-O-tetradecanoylphorbol-13-acetate (TPA) (PN:P8139, Sigma) for 48 hours prior to measurement [46]. In MCF-10A, EMT was induced by incubating cells in medium supplemented with 10 ng/mL TGF-β1 (PN:90900-1, BPSBioscience, San Diego, USA) one week prior to measurement [47–49]. For DU-145 and A-549, EMT was induced by 24 hours treatment with 5 ng/mL TGF-β1 [34, 35].

Experimental setup.
To prepare mitotic cells for AFM measurements, ≈10 000 cells were seeded in a cuboidal silicon cultivation chamber (0.56 cm^2 area, from cutting ibidi 12-well chamber) that was placed in a 35 mm cell culture dish (fluorodish FD35-100, glass bottom, World Precision Instruments) one day before the measurement so that a confluency of ≈30% was reached on the measurement day. Mitotic arrest by supplementing STC (Sigma) was induced 2 - 8 h before the measurement at a concentration of 2 µM. For measurement, mitotically arrested cells were identified by their shape. Their uncompressed diameter ranged typically from 18 to 23 µm.
To prepare AFM measurements of suspended interphase cells, cell culture dishes (fluorodish FD35-100) were coated by incubating the dish at 37 °C with 0.5 mg/mL Poly(L-Lysine)-PEG dissolved in PBS for 1 h (PLL(20)-g[3.5]-PEG(2), SuSoS, Dubendorf, Switzerland) to prevent cell adhesion. Prior to measurements, cultured cells were detached by the addition of 0.05% trypsin-EDTA (Invitrogen). Approximately 30 000 cells in suspension were placed in the coated culture dish.
The culture medium was changed to CO_2-independent DMEM (PN: 12800-017, Invitrogen) with 4 mM $NaHCO_3$ buffered with 20 µM HEPES/NaOH pH 7.2, for AFM experiments ≈2 h before the measurement [10, 21, 22, 50].
The experimental setup included an AFM (Nanowizard I, JPK Instruments) that was mounted on a Zeiss Axiovert 200M optical, wide-field microscope using a 20x objective (Zeiss, Plan Apochromat, NA = 0.8) along with a CCD camera (DMK 23U445 from Theimagingsource). Cell culture dishes were kept in a Petri dish heater (JPK Instruments) at 37 °C during the experiment. Prior to every experiment, the spring constant of the cantilever was calibrated by thermal noise analysis (built-in software, JPK) using a correction factor of 0.817 for rectangular cantilevers [51]. The cantilevers used were tipless, 200 - 350 µm long, 35 µm wide, and 2 µm thick (NSC12/tipless/no aluminium or CSC37/tipless/no aluminum, Mikromasch). The nominal force constants of the cantilevers ranged between 0.2 and 0.8 N/m. The cantilevers were supplied with a wedge, consisting of UV curing adhesive (Norland 63, Norland Products Inc.) to correct for the 10° tilt [52]. The measured force, piezo height, and time were output at a time resolution of 500 Hz.

Dynamic AFM-based cell confinement.
Preceding every cell compression, the AFM cantilever was lowered to the dish bottom in the vicinity of the cell until it touched the surface and then retracted to approximately 14 μm above the surface. Subsequently, the free cantilever was moved and placed on top of the cell. Thereupon, a bright-field image of the equatorial plane of the confined cell is recorded in order to evaluate the equatorial radius R_{eq} at a defined cell height h. Cells were confined between dish bottom and cantilever wedge. Then, oscillatory height modulations of the AFM cantilever were carried out with typical oscillation amplitudes of $0.1 - 0.5\,\mu$m in a frequency range of 0.02 and 2 Hz. During this procedure, the cell was on average kept at a normalised height $\tilde{h} = h/(2R)$ of $60 - 70\%$, where $R = (3/(4\pi)V)^{1/3}$ and V is the estimated cell volume. Height oscillations were set to an amplitude of $0.25\,\mu$m.

Estimating cellular shape and volume during AFM measurements.
For our analysis, we anticipate that confined cells adopt droplet shapes of minimal surface area as reported in [21]. Cell volume was estimated by imaging the equatorial plane of a confined cell at retracted AFM cantilever, i.e. of a cell height h of $\approx 14\,\mu$m. The cell volume was determined by the approximative formula $V = -\frac{\pi}{24}h(h^2(3\pi-10) - 6h(\pi-4)R_{eq} - 24R_{eq}^2)$ [22, 36]. For measurement analysis, the cell volume was anticipated to be constant during the measurement of the cell [21, 22]. Further, we estimated radii of principle curvatures R_1 and R_2 at the equator of the cell surface as $h/2$ and R_{eq} [22]. The area of contact between cells and cantilever was estimated as $A_{con} = \pi r_{con}^2$ with the contact radius $r_{\rm con}$ determined by the approximative formula $r_{\rm con} = (R_{eq} - \frac{h}{2}) + \frac{2}{3}\left(\sqrt{(2R_{eq}^3 - hR_{eq}^2)}/\sqrt{(h+2R_{eq})} - (R_{eq} - \frac{h}{2})\right)$ as described in [21].

Data analysis.
In our analysis, the force response of the cell is translated into an effective cortical tension $\gamma = F/\left[A_{con}(1/R_1 + 1/R_2)\right]$, where A_{con} is the contact area between confined cell and AFM cantilever and R_1 and R_2 are the radii of principal curvatures of the free surface of the confined cell [10, 21, 22]. Oscillatory force and cantilever height readouts were analysed in the following way; for every time point, effective cortical tension γ and surface area strain $(A(t) - \langle A\rangle)/\langle A\rangle$ were estimated. An amplitude and a phase angle associated to the oscillatory time variation of effective tension γ and surface area strain are extracted by sinusoidal fits. To estimate the value of the complex elastic modulus at a distinct frequency, we determine the phase angles φ_γ and φ_{ϵ_A} as well as amplitudes A_γ and A_{ϵ_A} of active cortical tension and surface area strain, respectively. The complex elastic modulus at this frequency is then calculated as $A_\gamma/A_{\epsilon_A}\exp^{i(\varphi_\gamma - \varphi_{\epsilon_A})}$.
Model Equations (2) and (3) were fitted to data of complex elastic moduli with a least square fit in Matlab using the command lsqcurvefit. Statistical analyses of cortex mechanical parameters were performed in Matlab using the commands 'boxplot' and 'ranksum' to generate boxplots and determine p-values from a Mann-Whitney U-test (two-tailed), respectively.

Model of cortical force response.
In steady state, at constant cantilever height, the obtained tension value γ is approximately constant in time and interpreted as the active cortical tension γ_{act}. If the cortical film is subject to dynamic deformation, the mechanical response of the cortex changes over time. We

assume a linear viscoelastic response of the form [22, 53]

$$\gamma(t) = \int_{-\infty}^{t} G(t-t')\dot{\epsilon}_A(t')dt' + \gamma_{act} \quad , \tag{1}$$

where $\epsilon_A(t) = (A(t) - A_0)/A_0$ is the area strain, A_0 is a reference area, and the dot indicates a time derivative. The relaxation modulus $G(t)$ shows the time-dependent response, which consists of memory effects due to viscoelastic material properties.
Measurement results obtained from mitotic HeLa cells put forward a relaxation spectrum $h(\tau) = K_h$ for $\tau \leq \tau_{max}$ and $h(\tau) = 0$ for $\tau > \tau_{max}$ for cortical material [22]. The corresponding relaxation modulus reads $G(t) = -K_h Ei(-t/\tau_{\max})$ where $Ei(z)$ is the exponential integral function [22]. The associated complex elastic modulus $G^*(\omega)$ is calculated as $G^*(\omega) = i\omega \int_0^\infty G(t)\, e^{-i\omega t}\, dt$. Adding a viscous contribution η to capture the viscous response of the cytoplasm or the medium in particular at high frequencies, we obtain the following functional form of storage and loss moduli

$$G'(\omega) = \frac{K_h}{2} \log(1 + (\tau_{max}\omega)^2) \tag{2}$$

$$G''(\omega) = K_h \arctan(\tau_{max}\omega) + \omega\eta \quad , \tag{3}$$

where $G^* = G' + iG''$. Eqn. (2) and (3) were used to perform the frequency-dependent fits in this paper. They constitute a simple model to discuss the rheology of the cortical layer based on a characteristic time scale τ_{max} and a complex elastic modulus K_h.

Western blotting
Protein expression in DU-145 and A-549 before and after EMT was analysed using Western blotting. Cells were seeded onto a 6-well plate and grown up to a confluency of 80-90% with or without EMT-inducing agents. Thereafter, cells were lysed in SDS sample/lysis buffer (62.5 mM TrisHcl pH 6.8, 2% SDS, 10% Glycerol, 50 mM DTT and 0.01%Bromophenolblue). Cell lysates were incubated for 30 mins with the lysis buffer at 4°C. Subsequently, they were sonicated for 1 mins to break-down undissolved components and then boiled for 5 minutes. 10 - 20 μL of the cleared lysate was then used for immunoblotting. The cleared lysates were first run on precast protein gels (PN:456-1096 or 456-1093, Bio-Rad) in MOPS SDS running buffer (B0001, Invitrogen). Subsequently, proteins were transferred to nitrocellulose membranes (Merck). Nitrocellulose membranes were blocked with 5% (w/v) skimmed milk powder (T145.1, Carl Roth, Karlsruhe, Germany) in TBST (20 mM/L Tris-HCl, 137 mM/L NaCl, 0.1% Tween 20 (pH 7.6)) for 1 h at room temperature followed by washing with TBST, and incubation at 4°C overnight with the corresponding primary antibody diluted 1:1000 (Vimentin, E-Cadherin), 1:500 (N-Cadherin) or 1:3000 (GAPDH) in 1% (w/v) bovine serum albumin/TBST solution. Thereupon, the blots were incubated with appropriate secondary antibodies conjugated to horseradish peroxidase, Rabbit anti-mouse HRP (PN: ab97045, Abcam) or Goat anti-rabbit HRP (PN: ab97051, Abcam) at 1:3000 dilution in 5% (w/v) skimmed milk powder in TBST for 1 h at room temperature. After TBST washings, specifically bound antibodies were detected using Pierce enhanced chemiluminescence substrate (ECL) (PN:32109, Invitrogen). The bands were visualised and analysed using a CCD-based digital blot scanner, ImageQuant LAS4000 (GE Healthcare Europe, Freiburg, Germany). Primary antibodies used are as follows: E-Cadherin (PN:60335-1-lg, Proteintech), N-Cadherin (PN:13116T, Cell Signaling Technology), Vimentin (PN:AMF-17b, Developmental Studies Hybridoma Bank, Iowa City, IA), GAPDH (PN:ab9485, Abcam).

Acknowledgments

We thank Marta Urbanska and Jochen Guck for provision of the cell line A-549. Further, we thank Isabel Richter, Ivan Antonenko and Rewati Limaye for support of western blotting work. E.F.-F. acknowledges financial support from the Deutsche Forschungsgemeinschaft, projects FI 2260/4-1 and FI 2260/5-1. K.H. and E.F.-F. were further supported by the Deutsche Forschungsgemeinschaft under Germany's Excellence Strategy, EXC-2068-390729961, Cluster of Excellence Physics of Life of TU Dresden.

Author Contributions

K.H. and E.F.-F. designed the research. K.H. and A.F. performed experiments. K.H. and E.F.-F. carried out the data analysis. K.H. and E.F.-F. wrote the manuscript.

Competing Interests

The authors declare no competing interests.

* Corresponding author: elisabeth.fischer-friedrich@tu-dresden.de

[1] Svitkina, T. M., 2020. Actin Cell Cortex: Structure and Molecular Organization. Trends Cell Biol 30:556–565.
[2] Janmey, P. A., and R. T. Miller, 2011. Mechanisms of mechanical signaling in development and disease. J Cell Sci 124:9–18.
[3] Salbreux, G., G. Charras, and E. Paluch, 2012. Actin cortex mechanics and cellular morphogenesis. Trends Cell Biol 22:536–545.
[4] Alberts, B., A. Johnson, J. Lewis, M. Raff, K. Roberts, and P. Walter, 2002. Molecular Biology of the Cell. Garland Science, 4th edition.
[5] Pecorino, L., 2016. Molecular Biology of Cancer: Mechanisms, Targets, and Therapeutics. Oxford University Press.
[6] Dongre, A., and R. A. Weinberg, 2019. New insights into the mechanisms of epithelial-mesenchymal transition and implications for cancer. Nat Rev Mol Cell Biol 20:69–84.
[7] Scheel, C., and R. A. Weinberg, 2012. Cancer stem cells and epithelial-mesenchymal transition: concepts and molecular links. Semin Cancer Biol 22:396–403.
[8] Felipe Lima, J., S. Nofech-Mozes, J. Bayani, and J. M. S. Bartlett, 2016. EMT in Breast Carcinoma-A Review. J Clin Med 5.
[9] Ilina, O., P. G. Gritsenko, S. Syga, J. Lippoldt, C. A. M. La Porta, O. Chepizhko, S. Grosser, M. Vullings, G.-J. Bakker, J. Starru, P. Bult, S. Zapperi, J. A. Ks, A. Deutsch, and P. Friedl, 2020. Cellcell adhesion and 3D matrix confinement determine jamming transitions in breast cancer invasion. Nat Cell Biol 22.
[10] Hosseini, K., A. Taubenberger, C. Werner, and E. FischerFriedrich, 2020. EMT-induced cell mechanical changes enhance mitotic rounding strength. Adv Sci 2001276.
[11] Bellovin, D. I., R. C. Bates, A. Muzikansky, D. L. Rimm, and A. M. Mercurio, 2005. Altered Localization of p120 Catenin During Epithelial to Mesenchymal Transition of Colon Carcinoma Is Prognostic for Aggressive Disease. Cancer Res 65:10938–10945.
[12] Huang, B., M. Lu, M. K. Jolly, I. Tsarfaty, J. Onuchic, and E. Ben-Jacob, 2014. The three-way switch operation of Rac1/RhoA GTPase-based circuit controlling amoeboid-hybrid-mesenchymal transition. Sci Rep 4.
[13] Chen, X., H. Cheng, T. Pan, Y. Liu, Y. Su, C. Ren, D. Huang, X. Zha, and C. Liang, 2015. mTOR regulate EMT through RhoA and Rac1 pathway in prostate cancer. Mol Carcinog 54:1086–1095.
[14] Guck, J., S. Schinkinger, B. Lincoln, F. Wottawah, S. Ebert, M. Romeyke, D. Lenz, H. M. Erickson, R. Ananthakrishnan, D. Mitchell, J. Ks, S. Ulvick, and C. Bilby, 2005. Optical deformability as an inherent cell marker for testing malignant transformation and metastatic competence. Biophys J 88:3689–3698.
[15] Lincoln, B., H. M. Erickson, S. Schinkinger, F. Wottawah, D. Mitchell, S. Ulvick, C. Bilby, and J. Guck, 2004. Deformability-based flow cytometry. Cytome A 59A:203–209.
[16] Xu, W., R. Mezencev, B. Kim, L. Wang, J. McDonald, and T. Sulchek, 2012. Cell Stiffness Is a Biomarker of the Metastatic Potential of Ovarian Cancer Cells. PLOS ONE 7:e46609.
[17] Lin, H.-H., H.-K. Lin, I.-H. Lin, Y.-W. Chiou, H.-W. Chen, C.-Y. Liu, H. I.-C. Harn, W.-T. Chiu, Y.-K. Wang, M.-R. Shen, and M.-J. Tang, 2015. Mechanical phenotype of cancer cells: cell softening and loss of stiffness sensing. Oncotarget 6:20946–20958.
[18] Cross, S. E., Y.-S. Jin, J. Rao, and J. K. Gimzewski, 2007. Nanomechanical analysis of cells from cancer patients. Nat Nanotechnol 2:780–783.
[19] Alibert, C., B. Goud, and J.-B. Manneville, 2017. Are cancer cells really softer than normal cells? Biol Cell 109:167–189.
[20] Fritsch, A., M. Hckel, T. Kiessling, K. D. Nnetu, F. Wetzel, M. Zink, and J. A. Ks, 2010. Are biomechanical changes necessary for tumour progression? Nat Phys 6.
[21] Fischer-Friedrich, E., A. A. Hyman, F. Jülicher, D. J. Müller, and J. Helenius, 2014. Quantification of surface tension and internal pressure generated by single mitotic cells. Sci Rep 4:6213.
[22] Fischer-Friedrich, E., Y. Toyoda, C. J. Cattin, D. J. Mller, A. A. Hyman, and F. Jlicher, 2016. Rheology of the Active Cell Cortex in Mitosis. Biophys J 111:589–600.
[23] Rother, J., H. Nding, I. Mey, and A. Janshoff, 2014. Atomic force microscopy-based microrheology reveals significant differences in the viscoelastic response between malign and benign cell lines. Open Biol 4:140046–140046.
[24] Wei, Z., S. Z, and S. Za, 2018. Epithelial-mesenchymal transition in breast epithelial cells treated with cadmium and the role of Snail. Toxicol Appl Pharmacol .
[25] Chao, Y. L., C. R. Shepard, and A. Wells, 2010. Breast carcinoma cells re-express E-cadherin during mesenchymal to epithelial reverting transition. Mol Cancer 9:179.
[26] Furtado, C., M. Marcondes, M. Sola-Penna, M. de Souza, and P. Zancan, 2012. Clotrimazole preferentially inhibits human breast cancer cell proliferation, viability and glycolysis. PLOS ONE .
[27] Thompson, E., S. Paik, N. Brünner, C. Sommers, G. Zugmaier, R. Clarke, T. Shima, J. Torri, S. Donahue, and M. Lippman, 1992. Association of increased basement membrane invasiveness with absence of estrogen receptor and expression of vimentin in human breast cancer cell lines. J Cell Physiol .
[28] Liu, Y.-L., C.-K. Chou, M. Kim, R. Vasisht, Y.-A. Kuo, P. Ang, C. Liu, E. P. Perillo, Y.-A. Chen, K. Blocher, H. Horng, Y.-I. Chen, D. T. Nguyen, T. E. Yankeelov, M.-C. Hung, A. K. Dunn, and H.-C. Yeh, 2019. Assessing metastatic potential of breast cancer cells based on EGFR dynamics. Sci Rep 9.
[29] Hurtley, S. M., 2020. Actin cortex controls cell migration. Science 368:1201–1203.

[30] Matthews, H. K., S. Ganguli, K. Plak, A. V. Taubenberger, Z. Win, M. Williamson, M. Piel, J. Guck, and B. Baum, 2020. Oncogenic Signaling Alters Cell Shape and Mechanics to Facilitate Cell Division under Confinement. Dev Cell 52:563–573.e3.

[31] Wang, Y., and B. P. Zhou, 2013. Epithelial-mesenchymal Transition—A Hallmark of Breast Cancer Metastasis. Cancer Hallm 1:38–49.

[32] Mickey, D. D., K. R. Stone, H. Wunderli, G. H. Mickey, and D. F. Paulson, 1980. Characterization of a human prostate adenocarcinoma cell line (DU 145) as a monolayer culture and as a solid tumor in athymic mice. Prog Clin Biol Res 37:67–84.

[33] Giard, D. J., S. A. Aaronson, G. J. Todaro, P. Arnstein, J. H. Kersey, H. Dosik, and W. P. Parks, 1973. In vitro cultivation of human tumors: establishment of cell lines derived from a series of solid tumors. J Natl Cancer Inst 51:1417–1423.

[34] Sun, Y., A. Schaar, P. Sukumaran, A. Dhasarathy, and B. B. Singh, 2018. TGFβ-induced epithelial-to-mesenchymal transition in prostate cancer cells is mediated via TRPM7 expression. Mol Carcinog 57:752–761.

[35] Suh, S.-S., J. Y. Yoo, R. Cui, B. Kaur, K. Huebner, T.-K. Lee, R. I. Aqeilan, and C. M. Croce, 2014. FHIT suppresses epithelial-mesenchymal transition (EMT) and metastasis in lung cancer through modulation of microRNAs. PLoS Genet 10:e1004652–e1004652.

[36] Mokbel, M., K. Hosseini, S. Aland, and E. Fischer-Friedrich, 2020. The Poisson Ratio of the Cellular Actin Cortex Is Frequency Dependent. Biophys J 118:1968–1976.

[37] Fischer-Friedrich, E., 2018. Active Prestress Leads to an Apparent Stiffening ofCells through Geometrical Effects. Biophys J 114:419–424.

[38] Ingber, D. E., N. Wang, and D. Stamenovic, 2014. Tensegrity, cellular biophysics, and the mechanics of living systems. Rep Prog Phys 77:046603.

[39] RocaCusachs, P., I. Almendros, R. Farr, and D. Navajas, 2006. Neutrophil microrheology probed by Atomic Force Microscopy. FASEB J 20:A1296–A1296.

[40] Lieleg, O., M. M. A. E. Claessens, Y. Luan, and A. R. Bausch, 2008. Transient Binding and Dissipation in Cross-Linked Actin Networks. Phys Rev Lett 101:108101. Publisher: American Physical Society.

[41] Broedersz, C. P., M. Sheinman, and F. C. MacKintosh, 2012. Filament-Length-Controlled Elasticity in 3D Fiber Networks. Phys Rev Lett 108:078102.

[42] Fritzsche, M., A. Lewalle, T. Duke, K. Kruse, and G. Charras, 2013. Analysis of turnover dynamics of the submembranous actin cortex. Mol Biol Cell 24:757–767.

[43] Osborne, L. D., G. Z. Li, T. How, E. T. O'Brien, G. C. Blobe, R. Superfine, and K. Mythreye, 2014. TGF-β1 regulates LARG and GEF-H1 during EMT to affect stiffening response to force and cell invasion. Mol Biol Cell 25:3528–3540.

[44] Schneider, D., T. Baronsky, A. Pietuch, J. Rother, M. Oelkers, D. Fichtner, D. Wedlich, and A. Janshoff, 2013. Tension Monitoring during Epithelial-to-Mesenchymal Transition Links the Switch of Phenotype to Expression of Moesin and Cadherins in NMuMG Cells. PLOS ONE 8:e80068.

[45] Haynes, J., J. Srivastava, N. Madson, T. Wittmann, and D. L. Barber, 2011. Dynamic actin remodeling during epithelial-mesenchymal transition depends on increased moesin expression. Mol Biol Cell 22:4750–4764.

[46] Kamiya, T., A. Goto, E. Kurokawa, H. Hara, and T. Adachi, 2016. Cross Talk Mechanism among EMT, ROS, and Histone Acetylation in Phorbol Ester-Treated Human Breast Cancer MCF-7 Cells. Oxid Med Cell Longev 2016:1284372–1284372.

[47] Zhang, P., Y. Wei, L. Wang, B. G. Debeb, Y. Yuan, J. Zhang, J. Yuan, M. Wang, D. Chen, Y. Sun, W. A. Woodward, Y. Liu, D. C. Dean, H. Liang, Y. Hu, K. K. Ang, M.-C. Hung, J. Chen, and L. Ma, 2014. ATM-mediated stabilization of ZEB1 promotes DNA damage response and radioresistance through CHK1. Nat Cell Biol 16:864–875.

[48] Xu, J., S. Lamouille, and R. Derynck, 2009. TGF-beta-induced epithelial to mesenchymal transition. Cell Res 19:156–172.

[49] Liang, Q., L. Li, J. Zhang, Y. Lei, L. Wang, D.-X. Liu, J. Feng, P. Hou, R. Yao, Y. Zhang, B. Huang, and J. Lu, 2013. CDK5 is essential for TGF-β1-induced epithelial-mesenchymal transition and breast cancer progression. Sci Rep 3:2932–2932.

[50] Stewart, M. P., J. Helenius, Y. Toyoda, S. P. Ramanathan, D. J. Müller, and A. A. Hyman, 2011. Hydrostatic pressure and the actomyosin cortex drive mitotic cell rounding. Nature 469:226–230.

[51] Butt, H. J., and M. Jaschke, 1995. Calculation of thermal noise in atomic force microscopy. Nanotechnology 6:1–7.

[52] Stewart, M. P., A. W. Hodel, A. Spielhofer, C. J. Cattin, D. J. Mller, and J. Helenius, 2013. Wedged AFM-cantilevers for parallel plate cell mechanics. Methods 60:186–194.

[53] Cordes, A., H. Witt, A. Gallem-Prez, B. Brckner, F. Grimm, M. Vache, T. Oswald, J. Bodenschatz, D. Flormann, F. Lautenschlger, M. Tarantola, and A. Janshoff, 2020. Prestress and Area Compressibility of Actin Cortices Determine the Viscoelastic Response of Living Cells. Phys Rev Lett 125:068101.